The Astrophysical Journal Letters, 981:L27 (16pp), 2025 March 10 https://doi.org/10.3847/2041-8213/adb48f

Measuring the Mean Free Path of H I Ionizing Photons at $3.2 \leqslant z \leqslant 4.6$ with DESI Y1 Quasars

Anning Gao[1], J. Xavier Prochaska[2,3,4], Zheng Cai[1], Siwei Zou[5,1], Cheng Zhao[1], Zechang Sun[1], S. Ahlen[6], D. Bianchi[7], D. Brooks[8], T. Claybaugh[9], A. de la Macorra[10], Arjun Dey[11], P. Doel[8], J. E. Forero-Romero[12,13], E. Gaztañaga[14,15], S. Gontcho A Gontcho[9], G. Gutierrez[16], K. Honscheid[17,18], S. Juneau[11], A. Kremin[9], P. Martini[18,19], A. Meisner[11], R. Miquel[20,21], J. Moustakas[22], A. Muñoz-Gutiérrez[10], J. A. Newman[23], I. Pérez-Ràfols[24], G. Rossi[25], E. Sanchez[26], M. Schubnell[27], D. Sprayberry[11], G. Tarlé[28], B. A. Weaver[11], and H. Zou[29]
[1] Department of Astronomy, Tsinghua University, Beijing 100084, People's Republic of China
[2] Department of Astronomy and Astrophysics, UCO/Lick Observatory, University of California, 1156 High Street, Santa Cruz, CA 95064, USA
[3] Kavli Institute for the Physics and Mathematics of the Universe (Kavli IPMU), 5-1-5 Kashiwanoha, Kashiwa 277-8583, Japan
[4] Division of Science, National Astronomical Observatory of Japan, 2-21-1 Osawa, Mitaka, Tokyo 181-8588, Japan
[5] Chinese Academy of Sciences South America Center for Astronomy, National Astronomical Observatories, CAS, Beijing 100101, People's Republic of China
[6] Physics Dept., Boston University, 590 Commonwealth Avenue, Boston, MA 02215, USA
[7] Dipartimento di Fisica "Aldo Pontremoli," Università degli Studi di Milano, Via Celoria 16, I-20133 Milano, Italy
[8] Department of Physics & Astronomy, University College London, Gower Street, London, WC1E 6BT, UK
[9] Lawrence Berkeley National Laboratory, 1 Cyclotron Road, Berkeley, CA 94720, USA
[10] Instituto de Física, Universidad Nacional Autónoma de México, Cd. de México C.P. 04510, México
[11] NSF NOIRLab, 950 N. Cherry Ave., Tucson, AZ 85719, USA
[12] Departamento de Física, Universidad de los Andes, Cra.1 No.18A-10, Edificio Ip, CP 111711, Bogotá, Colombia
[13] Observatorio Astronómico, Universidad de los Andes, Cra.1 No.18A-10, Edificio H, CP 111711 Bogotá, Colombia
[14] Institute of Cosmology and Gravitation, University of Portsmouth, Dennis Sciama Building, Portsmouth, PO1 3FX, UK
[15] Institut d'Estudis Espacials de Catalunya (IEEC), Esteve Terradas 1, Edifici RDIT, Campus PMT-UPC, 08860 Castelldefels, Spain
[16] Fermi National Accelerator Laboratory, PO Box 500, Batavia, IL 60510, USA
[17] Department of Physics, The Ohio State University, 191 West Woodruff Avenue, Columbus, OH 43210, USA
[18] Center for Cosmology and AstroParticle Physics, The Ohio State University, 191 West Woodruff Avenue, Columbus, OH 43210, USA
[19] Department of Astronomy, The Ohio State University, 4055 McPherson Laboratory, 140 W 18th Avenue, Columbus, OH 43210, USA
[20] Institut de Física d'Altes Energies (IFAE), The Barcelona Institute of Science and Technology, Campus UAB, 08193 Bellaterra Barcelona, Spain
[21] Institució Catalana de Recerca i Estudis Avançats, Passeig de Lluís Companys, 23, 08010 Barcelona, Spain
[22] Department of Physics and Astronomy, Siena College, 515 Loudon Road, Loudonville, NY 12211, USA
[23] Department of Physics & Astronomy and Pittsburgh Particle Physics, Astrophysics, and Cosmology Center (PITT PACC), University of Pittsburgh, 3941 O'Hara Street, Pittsburgh, PA 15260, USA
[24] Departament de Física, EEBE, Universitat Politècnica de Catalunya, c/Eduard Maristany10, 08930 Barcelona, Spain
[25] Department of Physics and Astronomy, Sejong University, Seoul, 143-747, Republic of Korea
[26] CIEMAT, Avenida Complutense 40, E-28040 Madrid, Spain
[27] Department of Physics, University of Michigan, Ann Arbor, MI 48109, USA
[28] University of Michigan, Ann Arbor, MI 48109, USA
[29] National Astronomical Observatories, Chinese Academy of Sciences, A20 Datun Rd., Chaoyang District, Beijing, 100012, People's Republic of China
Received 2024 November 24; revised 2025 February 6; accepted 2025 February 11; published 2025 March 5

Abstract

The mean free path of ionizing photons in the intergalactic medium (IGM; $\lambda_{\rm mfp}^{912}$) is a crucial quantity in modeling the ionization state of the IGM and the extragalactic ultraviolet background, and it is widely used in hydrodynamical simulations of galaxies and reionization. We construct the largest quasar spectrum data set to date —12,595 signal-to-noise ratio > 3 spectra—using the Y1 observations of the Dark Energy Spectroscopic Instrument, to make the most precise model-independent measurement of the mean free path at $3.2 \leqslant z \leqslant 4.6$. By stacking the spectra in 17 redshift bins and modeling the Lyman-continuum profile, we get a redshift evolution $\lambda_{\rm mfp}^{912} \propto (1+z)^{-4.27}$ at $2 \leqslant z \leqslant 5$, which is much shallower than the previous estimate, $\lambda_{\rm mfp}^{912} \propto (1+z)^{-5.4}$. We then explore the sources of systematic bias, including the choice of the intrinsic quasar continuum, the consideration of Lyman-series opacity and Lyman-limit opacity evolution, and the definition of $\lambda_{\rm mfp}^{912}$. Combining our results with estimates of $\lambda_{\rm mfp}^{912}$ at higher redshifts, we conclude at high confidence that the evolution in $\lambda_{\rm mfp}^{912}$ steepens at $z \approx 5$. We interpret this inflection as the transition from the end of H I reionization to a fully ionized plasma that characterizes the IGM of the past $\sim$10 billion yr.

Unified Astronomy Thesaurus concepts: Intergalactic medium (813); Quasar absorption line spectroscopy (1317); Reionization (1383); Observational cosmology (1146)

1. Introduction

The bulk of gas existing in the vast space between galaxies, commonly referred to as the intergalactic medium (IGM), is highly ionized after the epoch of reionization (J. E. Gunn & B. A. Peterson 1965). It is believed that ionizing photons from quasars and star-forming galaxies, which generate the extragalactic ultraviolet background (EUVB), play a crucial role in ionizing the neutral hydrogen in the IGM (X. Fan et al. 2006; C.-A. Faucher-Giguère et al. 2008a; L. L. Cowie et al. 2009; G. D. Becker & J. S. Bolton 2013; P. Madau & F. Haardt 2015; L. Jiang et al. 2022). Hydrodynamical simulations also rely on

the EUVB, as they provide an important source of heating and photoionization to the ionized plasma (e.g., B. D. Oppenheimer & R. Davé 2006; J. S. Bolton & M. G. Haehnelt 2007; J. Schaye et al. 2015; R. S. Somerville & R. Davé 2015; R. Davé et al. 2019; B. Villasenor et al. 2021).

To estimate the EUVB, except the photon emissivity of quasars and galaxies, it is necessary to measure the H I Lyman-limit opacity, frequently described by the mean free path of ionizing photons (F. Haardt & P. Madau 1996, 2012). Previous studies have used various methods to measure the mean free path. Observations of high-redshift quasar spectra showed the existence of the Lyα forest, which is composed of a series of H I absorbers blueward of the rest frame of the Lyα emission line that follows the underlying matter distribution (M. Rauch 1998). The mean free path can be calculated by integrating the distribution of column densities of these absorbers and its redshift evolution, $f(N_{\rm HI}, z) = \partial^2 n/(\partial N_{\rm HI}\partial z)$ (e.g., A. Meiksin & P. Madau 1993; C.-A. Faucher-Giguère et al. 2009; J. X. Prochaska et al. 2010; G. C. Rudie et al. 2013). However, this method relies on the assumption of the random placement of absorbers, thus it suffers from uncertainties from line blending and absorber clustering (J. X. Prochaska et al. 2014).

Another method that directly measures the mean free path exploits the composite of a large sample of quasar spectra, which has been proved to significantly reduce the uncertainties (J. X. Prochaska et al. 2009). Using this method, the mean free path has been measured at $2 \lesssim z \lesssim 5$, with spectra from both ground-based and space-based telescopes, yielding $\lambda_{\rm mfp}^{912} \propto (1+z)^{-5.4}$ (J. X. Prochaska et al. 2009; M. Fumagalli et al. 2013; J. M. O'Meara et al. 2013; G. Worseck et al. 2014), while other measurements show a slightly shorter $\lambda_{\rm mfp}^{912}$ at $z \sim 2.2$ (E. Lusso et al. 2018). Recently, the mean free path has been used to probe the end of reionization, by taking into account the quasar proximity effect, which suggests a much steeper evolution at $z \gtrsim 5$, indicative of a late-ending reionization model (G. D. Becker et al. 2021; C. Cain et al. 2021; P. Gaikwad et al. 2023; Y. Zhu et al. 2023; F. B. Davies et al. 2024; J. T. Roth et al. 2024). The mean free path can also be constrained from the individual quasar sightlines, e.g., by comparing between the flux ratios blueward and redward of the Lyman limit (M. Romano et al. 2019) or finding the Lyman-limit systems (LLSs) closest to the emitting quasar from the absorption of the first six transitions of the Lyman series, which is less robust due to the contamination of foreground absorbers (S. E. I. Bosman 2021).

The Dark Energy Spectroscopic Instrument (DESI; DESI Collaboration et al. 2016a, 2016b) started the first year of its main survey in 2021 May and finished in 2022 June. As a Stage-IV spectroscopic survey, DESI observed approximately 1.4 million quasars during the first year (Y1) of its main survey (DESI Collaboration et al. 2025, in preparation). This achievement has resulted in today's largest quasar spectroscopic catalog and enables today's most precise measurements of dark energy and large-scale structures (DESI Collaboration et al. 2024a, 2025a, 2025b). The large sample from DESI provides a great opportunity to measure the mean free path more precisely. In this Letter, we use DESI Y1 quasar spectra to measure the mean free path at $3.2 \leqslant z \leqslant 4.6$, employing the updated statistical methods of J. X. Prochaska et al. (2009; hereafter, P09). Thanks to the order-of-magnitude-larger sample size compared with the Sloan Digital Sky Survey (SDSS) I and SDSS-II (D. P. Schneider et al. 2010; used in P09), we obtain the measurements with an uncertainty $\sim$70% lower than previous work. Our updated values of the mean free path show a smoother redshift evolution compared with G. Worseck et al. (2014; hereafter, W14) and can be useful in establishing a more precise model of the EUVB.

The rest of the Letter is organized as follows. In Section 2, we will briefly introduce the characteristics of DESI spectra and discuss how we selected the quasar samples from its Y1 data set. In Section 3, we will describe our methodology in detail, including the stacking of spectra, the theoretical model, and the fitting method. We will present our results in Section 4. We discuss how our refined results of the mean free path could impact the modeling of other aspects of astrophysics and cosmology, particularly the modeling of reionization, in Section 5, and we summarize our conclusions in Section 6. Unless otherwise specified, a flat ΛCDM cosmology is adopted, with $\Omega_m = 0.3$, $\Omega_\Lambda = 0.7$, and $H_0 = 70\,{\rm km\,s^{-1}\,Mpc^{-1}}$; all the distances are proper distances, unless stated otherwise. For convenience, we also define the unitless h_{70} to be the Hubble constant in units of $70\,{\rm km\,s^{-1}\,Mpc^{-1}}$, which is used in our display of $\lambda_{\rm mfp}^{912}$ measurements.

2. Data

In this section, we first summarize the properties of DESI quasars and their spectra, and we discuss the potential bias that could affect our result. Then we introduce our criteria for selecting our quasar sample from DESI.

2.1. The DESI Quasar Sample

DESI was installed on the 4 m Mayall telescope at Kitt Peak, Arizona, along with 5000 fibers and fiber positioners. It employs three spectrographs, to obtain spectra simultaneously, commonly referred to as "*b*" (360–593 nm), "*r*" (560–772 nm), and "*z*" (747–980 nm), with the FWHM resolution $\lambda/\Delta\lambda$ ranging from 2000 (blue end) to 5500 (red end; DESI Collaboration et al. 2022). The observations are divided into dark, bright, and backup programs, according to the observing conditions, and quasars are observed in the dark program with an effective exposure time of $\sim$1000 s (E. F. Schlafly et al. 2023). CCD images are then processed to give a common $0.8\,{\rm \AA\,pixel^{-1}}$ wavelength grid for all spectra (J. Guy et al. 2023).

A complete and not biased quasar sample is crucial for our analysis. Here, we briefly summarize the main procedure and results of the DESI quasar target selection and validation (E. Chaussidon et al. 2023). DESI incorporates the optical photometry data of the *grz* bands from the Beijing–Arizona Sky Survey, the Mayall *z*-band Legacy Survey, and the Dark Energy Camera Legacy Survey, as well as the near-infrared photometry data of the W1 and W2 bands from the WISE satellite (A. Dey et al. 2019), based on which a random forest algorithm is designed to select quasars in the magnitude range $16.5 < r < 23$. In parallel, other criteria (e.g., source morphology) were tested during the survey validation (D. M. Alexander et al. 2023; DESI Collaboration et al. 2024b), to better select faint quasars and high-*z* quasars. The final quasar catalog is constructed after a template-fitting algorithm REDROCK (A. Anand et al. 2024; S. J. Bailey 2025, in preparation),[30] a broad Mg II line finder, and a deep convolutional neural network QuasarNet (N. Busca & C. Balland 2018) are successively applied to the observed

[30] https://github.com/desihub/redrock/

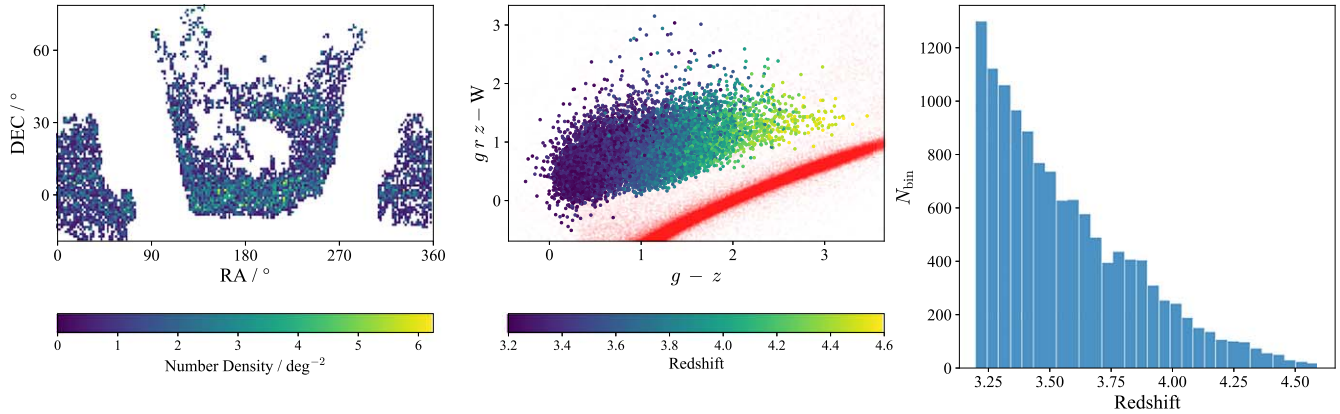

Figure 1. Parameter distributions of the DESI quasar sample analyzed here. Left: the distribution of angular positions, showing a roughly uniform distribution across the survey area. Middle: the distribution of quasar magnitude and color, colored with redshift. The x-axis is the $g-z$ color, and the y-axis is the color defined in E. Chaussidon et al. (2023), which combines the optical grz bands and the infrared W1 and W2 bands. To better illustrate the stellar contaminants, we use red points to represent the stellar color from the early data release of the DESI Milky Way Survey (S. E. Koposov et al. 2024), filtered with RVS_WARN = 0 and RR_SPECTYPE = 0, as well as PRIMARY = TRUE (see their Section 5.1). Right: the distribution of redshift. $N_{\rm bin}$ means the number of quasar sightlines within the redshift bin.

spectra, with the redshift determined at the same time. The overall procedure finally achieves >99% efficiency, >98% purity, and an approximately 60 deg^{-2} target density for $z>2.1$ quasars (E. Chaussidon et al. 2023).

Despite the excellent performance of the DESI target selection pipeline, we stress that there may still be possible biases that could affect our measurement. One of the main biases could be the quasar color selection. As discussed in G. Worseck & J. X. Prochaska (2011), the color selection criterion of SDSS selects $3\lesssim z\lesssim 3.5$ quasars that are systematically redder on $u-g$ color and have more intervening LLSs; this is due to the difficulty of distinguishing quasars from stars in this redshift range and causes the underestimation of the mean free path measured in P09. As we can see in Figure 1, stellar contamination still exists in DESI data at $3\lesssim z\lesssim 3.5$, and there is still the lack of a detailed study of DESI quasar selection bias. However, in this work, we treat the DESI sample as unbiased, since the infrared observations, the more advanced random forest algorithm, and the color-independent quasar variability are incorporated in the DESI main selection (E. Chaussidon et al. 2023). We still remain cautious about the potential biases, and careful examination is needed in future studies.

2.2. Sample Selection

We select our sample of 12,595 quasars from the main survey dark program of the DESI Y1 observation. In particular, we apply the following selection rules:

1. $3.2\leqslant z\leqslant 4.6$, where the redshift is determined by REDROCK. This range is set by our measuring method. As we will see in Section 3, our method requires the stacking of spectra and the fitting of the spectrum below the rest-frame Lyman limit (912 Å). Only a small number of $z>4.6$ quasars meet the other rules, which were deemed insufficient for stacking. Below $z<3.2$, quasars have a very short spectrum below the rest-frame Lyman limit, which is too little for robust fitting.
2. ZWARN = 0, to avoid problematic redshift determination, where ZWARN is one of the outputs of REDROCK (J. Guy et al. 2023; DESI Collaboration et al. 2024b, 2024c).
3. Avoid broad-absorption-line (BAL) systems. Specifically, we require that the intrinsic absorption index (P. B. Hall et al. 2002) and the balnicity index (R. J. Weymann et al. 1991) of C IV and S IIV are all zero, as derived from the future Data Release 1 of the BAL catalog and calculated using the methods in S. Filbert et al. (2024).
4. The signal-to-noise ratio (S/N) is larger than 3, where the S/N is estimated using the average pixel-level S/N at the rest-frame wavelength range 1450–1470 Å. Following P09, this rule is meant to decrease the variation in the stacking spectra. We also construct other samples for S/N cuts of 5, 7, and 10 to perform our following fitting procedures, and our results are shown to be insensitive to the selection of the S/N cut.

After selection, the official pipeline[31] is used to combine the three cameras. The galactic extinction is corrected both for flux and error to maintain the S/N, using the extinction function in J. A. Cardelli et al. (1989; $R_V=3.1$) and the dust extinction map in D. J. Schlegel et al. (1998). Distributions of angular location, color, and redshift of our sample are summarized in Figure 1. For comparison, we also list the measurements without this correction in Table 1, which mostly show a difference of less than 1σ and do not have a significant impact on the fitting. Therefore, we will not use these measurements in what follows.

3. Methodology

In this section, we detail our technique for obtaining mean free path measurements. Following W14, we define the mean free path as the mean distance that the ionizing photons will travel before suffering a $1/e$ amount of attenuation, where e is the base of natural logarithms.

3.1. Stacking

Since the mean free path is a statistical quantity, the stacking of spectra is important to our analysis. Here, we follow the procedures in J. M. O'Meara et al. (2013). We divide the quasar sample into 17 redshift bins, with 1000 or 500 quasars

[31] https://github.com/desihub/desispec

Table 1
$\lambda_{\rm mfp}^{912}$ Measurements

$z_{\rm min}$	$z_{\rm max}$	$z_{\rm median}$	$z_{\rm mean}$	$N_{\rm qso}$	λ_r range	$\lambda_{\rm mfp}^{912}$ with T02 SED	$\lambda_{\rm mfp}^{912}$ with L15 SED
3.200	3.236	3.217	3.218	1000	857–912 Å	65.4(64.7) ± 3.44	59.7 ± 2.83
3.236	3.275	3.255	3.255	1000	850–912 Å	64.6(62.7) ± 2.87	59.1 ± 2.38
3.275	3.320	3.297	3.297	1000	842–912 Å	66.5(65.2) ± 3.01	60.5 ± 2.49
3.320	3.364	3.341	3.342	1000	834–912 Å	60.1(59.0) ± 2.58	55.1 ± 2.16
3.364	3.415	3.389	3.389	1000	825–912 Å	63.3(61.4) ± 2.72	57.6 ± 2.24
3.415	3.474	3.443	3.444	1000	816–912 Å	60.6(59.3) ± 2.41	55.3 ± 2.00
3.474	3.539	3.506	3.506	1000	805–912 Å	52.0(50.9) ± 1.96	48.0 ± 1.68
3.539	3.613	3.577	3.576	1000	800–912 Å	50.4(49.2) ± 1.77	46.6 ± 1.51
3.613	3.696	3.653	3.653	1000	800–912 Å	47.1(46.4) ± 1.64	43.7 ± 1.42
3.696	3.756	3.724	3.725	500	800–912 Å	43.7(43.1) ± 2.06	40.7 ± 1.78
3.756	3.808	3.782	3.783	500	800–912 Å	41.4(40.9) ± 1.97	38.6 ± 1.72
3.808	3.866	3.837	3.837	500	800–912 Å	41.3(40.6) ± 2.11	38.5 ± 1.85
3.866	3.931	3.896	3.897	500	800–912 Å	35.4(34.7) ± 1.73	33.3 ± 1.53
3.931	4.024	3.976	3.976	500	800–912 Å	35.9(35.2) ± 1.52	33.7 ± 1.35
4.024	4.161	4.082	4.085	500	800–912 Å	31.6(31.1) ± 1.38	29.8 ± 1.23
4.161	4.434	4.270	4.278	500	800–912 Å	29.5(28.8) ± 1.15	27.8 ± 1.03
4.434	4.600	4.489	4.498	95	800–912 Å	23.5(23.5) ± 1.90	22.4 ± 1.72
A						35.03(34.33) ± 0.54	32.92 ± 0.47
η						−4.03(−4.06) ± 0.16	−3.84 ± 0.14

Note. The unit of $\lambda_{\rm mfp}^{912}$ and A is h_{70}^{-1} Mpc. The values in the brackets are measured without correction for Galactic extinction. The parameters A and η are fitted using median redshifts.

in each bin, except that the last one has 95 quasars. The reason why the higher-redshift bins have only 500 quasars instead of 1000 is that we want to keep a balance between the redshift uncertainty and the $\lambda_{\rm mfp}^{912}$ uncertainty. The detailed information of each bin is shown in Table 1. For each redshift bin, the spectra are shifted to the quasar's rest frame and normalized with the median flux at 1450–1470 Å. Since the wavelength grid size after redshift shifting is $0.8\,\text{Å}/(1+z_{\rm qso}) < 0.2$ Å for all the spectra, where $z_{\rm qso}$ is the quasar redshift, we choose a 0.5 Å pixel^{-1} wavelength grid for stacking, ensuring that for each pixel in the stacked spectra, there is at least one pixel from every original spectrum that can be stacked into that pixel. The stacked flux is chosen to be the mean of the stacked pixels. The stacked flux uncertainty is calculated as

$$\sigma_{\rm stacked} = \frac{1}{n}\sqrt{\sigma_1^2 + \sigma_2^2 + \cdots + \sigma_n^2}, \quad (1)$$

i.e., we treat the flux as an independent Gaussian distribution (for the independence, see J. Guy et al. 2023, Section 4.5). We give every sightline an equal stacking weight, as each sightline represents a spatial direction that should be treated equally. All the pixels with a nonzero MaskBit are neglected during stacking. We stress that we do not use the inverse-variance weighting. Although it would of course reduce the variance of our composite spectra, it would also introduce an unwanted prior that gives high-S/N sightlines more weight and may bias our result. Figure 2 shows several examples of our stacked spectra.

To estimate the sample variance and the uncertainties introduced by redshift error, we use the bootstrap technique. For each redshift bin, a random sample is generated from the quasars of this bin, allowing for duplication. Then each spectrum's redshift allows for a random Gaussian change, with zero mean and the standard deviation of the redshift error equivalent to 350 km s^{-1}, which is inspired by the visual inspection results of the DESI quasars (D. M. Alexander et al. 2023). Those spectra are stacked using the procedures described before and share the same wavelength grid as the previous stacks. This process is performed 1000 times, and 1000 different stacks are generated, which are then used to perform Markov Chain Monte Carlo (MCMC) analysis, as described in Section 3.3.

3.2. Modeling

We use the technique in P09 to analyze the stacked spectrum at $\lambda < 912$ Å, which has been widely used in previous mean free path measurements (M. Fumagalli et al. 2013; J. M. O'Meara et al. 2013; W14; E. Lusso et al. 2018). This portion of the spectrum is modeled to be the intrinsic spectral energy distribution (SED) attenuated by the Lyman-series effective optical depth, $\tau_{\lambda_r}^{\rm LyS}$, which is caused when the photons with rest-frame wavelength λ_r are redshifted to a specific Lyman-series line (Lyα, Lyβ, etc.) and Lyman-continuum effective optical depth, $\tau_{\lambda_r}^{\rm LyC}$, which is caused when the photon's wavelength is shorter than 912 Å, so that it can ionize HI atoms. We can write down the explicit expression

$$f_{\lambda_r} = f_{\lambda_r}^{\rm SED} \exp(-\tau_{\lambda_r}^{\rm LyS}) \exp(-\tau_{\lambda_r}^{\rm LyC}), \quad (2)$$

where f_{λ_r} is the observed composite spectrum and $f_{\lambda_r}^{\rm SED}$ is the intrinsic quasar SED. The three parts of Equation (2) are modeled as follows, following J. M. O'Meara et al. (2013), W14, and E. Lusso et al. (2018). (i) The quasar SED is assumed to be a template modified by a power law:

$$f_{\lambda_r}^{\rm SED} = f_0 f_{\lambda_r}^{\rm tem} \left(\frac{\lambda_r}{912\ \text{Å}}\right)^{-\alpha}, \quad (3)$$

where α is the tilt index, f_0 is a normalization factor accounting for the continuum uncertainty, and $f_{\lambda_r}^{\rm tem}$ is the SED template. We do not include the sky zero-point as a free parameter in our

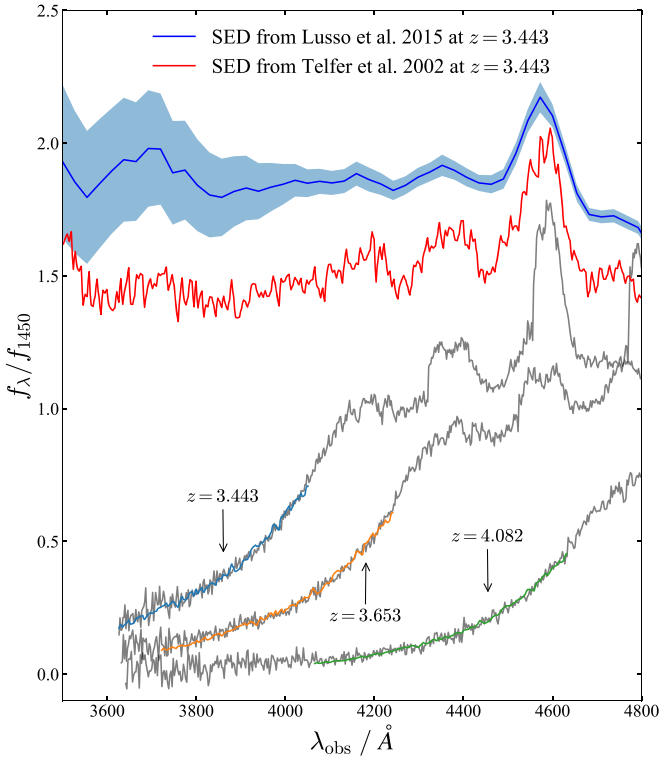

Figure 2. Examples of our stacked spectra. The gray spectra are the $z_{\rm median} = 3.443$ (left), $z_{\rm median} = 3.653$ (middle), and $z_{\rm median} = 4.083$ (right) stacks, shifted to the observation frame. Overplotted are the best-fit models. The red spectrum is the T02 SED, and the blue spectrum at the top is the L15 SED, with the lighter blue region indicating the 1σ confidence region. The two SEDs are both shifted to $z_{\rm qso} = 3.443$, to be comparable with the leftmost stack. All five spectra are normalized at 1450 Å. Overplotted on the DESI stacked spectra are the best-fit models using the T02 SED. An illustration of the composite spectra and SED templates redward of Lyman-α is shown in Appendix A.

above formalism, because our fitted f_0 is very close to 1 in all our fittings. Therefore, the effect of the sky zero-point uncertainty is accounted for in f_0 to a first-order approximation. R. C. Telfer et al. (2002; hereafter, T02) and E. Lusso et al. (2015; hereafter, L15) both stacked quasar spectra from the Hubble Space Telescope (HST) and obtained average SEDs differing by ∼30% at the Lyman continuum. For comparison, we use the SED template from both composites and show the results in Table 1. The base of the power-law modification is chosen to be 912 Å instead of the widely used 1450 Å, because we only want this modification to impact the slope of the SED at the Lyman continuum, and a 1450 Å base would introduce an additional overall normalization at the Lyman continuum that could be degenerate with f_0.

(ii) The Lyman-series optical depth is described by a power law:

$$\tau_{\lambda_r}^{\rm LyS} = \tau_0^{\rm LyS}\left(\frac{1+z_{912}}{1+z_{\rm qso}}\right)^{\gamma_\tau}, \tag{4}$$

where $z_{\rm qso}$ is the quasar redshift and is represented by the median redshift of the stacked spectra (the mean redshift is similar, as shown in Table 1, so the freedom of choosing the median or mean would not introduce any inconsistency) and z_{912} is defined as

$$1 + z_{912} = \frac{\lambda_r}{912\ \text{Å}}(1 + z_{\rm qso}), \tag{5}$$

i.e., z_{912} represents the redshift at which the λ_r photon is shifted to 912 Å. This power law is inspired by J. X. Prochaska et al. (2014), and the index γ_τ is chosen to be 3 for all redshift bins, as justified in Appendix B. In practice, the coefficient $\tau_0^{\rm LyS}$ is determined by the absorption at rest frame 912 Å. We stress that this term is the key difference between our measurements and the analysis in P09, where the authors only considered the Lyman-continuum opacity and measured a mean free path systematically higher than ours. A detailed explanation is given in Section 4.

(iii) The Lyman-limit optical depth is described by P09 and J. M. O'Meara et al. (2013):

$$\tau_{\lambda_r}^{\rm LyC} = \int \kappa\, dr, \tag{6}$$

where κ is the opacity coefficient, whose redshift evolution and frequency dependence is modeled separately:

$$\begin{aligned}\kappa &= \kappa_0\left(\frac{1+z}{1+z_{\rm qso}}\right)^{\gamma_\kappa}\left(\frac{\nu}{\nu_{912}}\right)^{-2.75}\\ &= \kappa_0\left(\frac{1+z}{1+z_{\rm qso}}\right)^{\gamma_\kappa}\left(\frac{1+z}{1+z_{912}}\right)^{-2.75},\end{aligned} \tag{7}$$

where ν_{912} is the Lyman-limit frequency and dr is modeled with cosmology:

$$\begin{aligned}\frac{dr}{dz} &= \frac{c}{H_0}\frac{1}{(1+z)\sqrt{\Omega_m(1+z)^3+\Omega_\Lambda}}\\ &\approx \frac{c}{H_0\sqrt{\Omega_m}}(1+z)^{-2.5}.\end{aligned} \tag{8}$$

The Universe is matter-dominated at $3 < z < 5$, which justifies the last approximation in the above equation. Combining the three equations, we get:

$$\begin{aligned}\tau_{\lambda_r}^{\rm LyC} = &\frac{c\kappa_0}{H_0\sqrt{\Omega_m}}\frac{(1+z_{912})^{2.75}}{(1+z_{\rm qso})^{\gamma_\kappa}}\\ &\times\int_{z_{912}}^{z_{\rm qso}}(1+z)^{\gamma_\kappa-5.25}\,dz.\end{aligned} \tag{9}$$

In conclusion, there are three parameters in our model that can be fitted: the normalization factor f_0, the "effective" opacity coefficient $\kappa_{912} \equiv c\kappa_0/(H_0\sqrt{\Omega_m})$, and the evolution index γ_κ. To simplify our model, we assume $\gamma_\kappa = \alpha = 0$. This is for two reasons: first, in our redshift range, the opacity does not evolve rapidly; and second, for the fitted wavelength range, the spectrum's decline is dominated by opacity, and unless there is an extreme tilt (e.g., $|\alpha| > 0.5$), the result will not be highly influenced by it.

Finally, our definition of $\lambda_{\rm mfp}^{912}$ corresponds to a photon that has a specific emission wavelength λ_r and experiences a total Lyman-limit optical depth $\tau_{\lambda_r}^{\rm LyC} = 1$, from $z_{\rm qso}$, where the photon is emitted, to z_{912}, where the photon is redshifted enough to have $h\nu < 1$ Ryd. Thereby, $\lambda_{\rm mfp}^{912}$ is defined to be the

physical distance between $z_{\rm qso}$ and z_{912} for these photons:

$$\lambda_{\rm mfp}^{912} \equiv \int c\, dt = \int_{z_{912}}^{z_{\rm qso}} \frac{c\, dz}{H(z)(1+z)}. \quad (10)$$

3.3. Fitting

We use the MCMC technique to estimate the posterior distribution of the parameters for the composite spectra in each redshift bin. To better combine the uncertainty introduced by spectrum fluctuations, sample selection, and redshift estimation, we perform MCMC analysis for each bootstrap spectrum and combine all the posteriors with equal weights to give the final posterior. We choose the traditional form of the χ^2 likelihood:

$$\chi^2 = \sum_i \left(\frac{f_i - f_i^{\rm model}}{\sigma_i} \right)^2, \quad (11)$$

where f_i and $f_i^{\rm model}$ are the stacked flux and the model flux at the ith pixel, respectively, and the uncertainty σ_i is defined in Equation (1) and chosen to be the same for all the bootstrap spectra in each redshift bin, to reduce the computational cost. We do not choose to represent the sample variance with the covariance matrix calculated from the bootstrap spectra, as we discovered that this would underestimate the final uncertainties of $\lambda_{\rm mfp}^{912}$, which may probably be caused by the ignorance of non-Gaussian variance. In our fiducial model, the prior is chosen to be a uniform distribution with a loose boundary $0 < f_0 < 3$, $0 < \kappa_{912} < 1000$. The lower bound of the fitted spectral region is the maximum between 800 Å and the shortest wavelength that has a contribution from all of the stacked spectra.

An example of combined posterior distributions is shown in in Appendix C, together with the mean free path distribution calculated from 200,000 sample points. Although the combined posterior is not strictly Gaussian, the marginal distributions of the parameters and the mean free path distribution are still symmetric and can be viewed as an imperfect Gaussian shape. Therefore, the fitted value of the mean free path is chosen to be the median, and the uncertainty is chosen to be the standard deviation, which corresponds to the 68% confidence level.

4. Results

Following the method, we fit the mean free paths of 17 redshift bins using the stacked spectra from 12,595 quasars. All the fitted values are shown in Table 1, where only the statistical uncertainties given by MCMC are included in the error bars. In Section 4.1, we explore the redshift evolution of the mean free path and discuss how our results differ from previous measurements, which are listed in Appendix D. In Section 4.2, we validate our results and discuss the possible systematic uncertainties in our measurements.

4.1. Redshift Evolution of the Mean Free Path

The redshift evolution of the mean free path plays a crucial role in understanding the evolution of the thermal state of the IGM and determining the content of cosmic residual neutral hydrogen at the post-reionization epoch. W14 provides a comprehensive collection of $\lambda_{\rm mfp}^{912}$ and gives $\lambda_{\rm mfp}^{912} \propto (1+z)^{-5.4\pm0.4}$, which is much steeper than the speed caused by cosmic expansion only and indicates the decrease of the number and/or size of absorbers. This evolution is also consistent with hydrodynamical simulations in A. D'Aloisio et al. (2020), where the IGM is fully ionized and relaxed. E. Lusso et al. (2018), however, suggest a slower evolution of the mean free path, $\lambda_{\rm mfp}^{912} \propto (1+z)^{-4.5\pm0.2}$, incorporating the new measurements with an updated quasar SED.

In recent years, mean free path measurements have been extended to higher redshifts, where the mean free path becomes too short to neglect the proximity effect of quasars. This effect is caused by the extra ionization of neutral hydrogen from the nearby quasars and may bias the mean free path measurements, as the local effects dominate and do not reflect the opacity of the entire IGM. G. D. Becker et al. (2021) and Y. Zhu et al. (2023) measure the mean free path at $5 \lesssim z \lesssim 6$, by considering the size of the quasar proximity zone, and their measurements imply a much steeper evolution of the mean free path at this redshift range.

Here, we present our measurements of the mean free path using the T02 SED as a function of redshift in Figure 3, together with previous measurements at $z \lesssim 5$. The T02 results are used as the fiducial results throughout the rest of this Letter, as most previous measurements at similar redshifts—e.g., P09, M. Fumagalli et al. (2013), J. M. O'Meara et al. (2013), and W14—all used the T02 SED, and employing the same SED will help us maintain consistency and compare with these results. We also fit the two-parameter model in W14, $\lambda_{\rm mfp}^{912} = A[(1+z)/5]^{\eta}$, using MCMC and our data only and get $A = 35.03 \pm 0.54\, h_{70}^{-1}$ Mpc and $\eta = -4.03 \pm 0.16$. The two parameters fitted with our other measurements are shown in the bottom lines in Table 1.

Our measurements show several major differences comparing with the previous ones:

1. The uncertainties are significantly reduced due to our large sample. However, as shown in Table 1, although we use 1000 spectra for stacking for the first nine redshift bins and less spectra for the others, the $\lambda_{\rm mfp}^{912}$ uncertainties seem not to show corresponding smaller values for the first nine bins, which may call into question the necessity of employing such a large sample. We admit that it is indeed not clear, if we look at the absolute value, but this is not the case if we look at the relative uncertainties. As shown in Figure 4, the first nine bins do exhibit smaller relative uncertainties, especially if we compare the eighth and ninth points with the 10th and 11th points. The seemingly large relative uncertainties for the first seven bins are mainly due to the shorter rest-frame wavelength range that we use for the fit, since a shorter wavelength range gives less spectrum points available for the fitting and thus limits the constraining power.
2. The measured mean free paths are systematically lower than previous estimates, especially P09. The discrepancy occurs mostly at $z \lesssim 4$, and the four points with the lowest redshifts in our measurements are only ∼75% of the corresponding values of the W14 power law. The discrepancy implies a systematic bias induced from either the data collection, i.e., the different target selections of DESI and SDSS, or the different fitting procedure. We explore a number of possibilities in the next subsection.

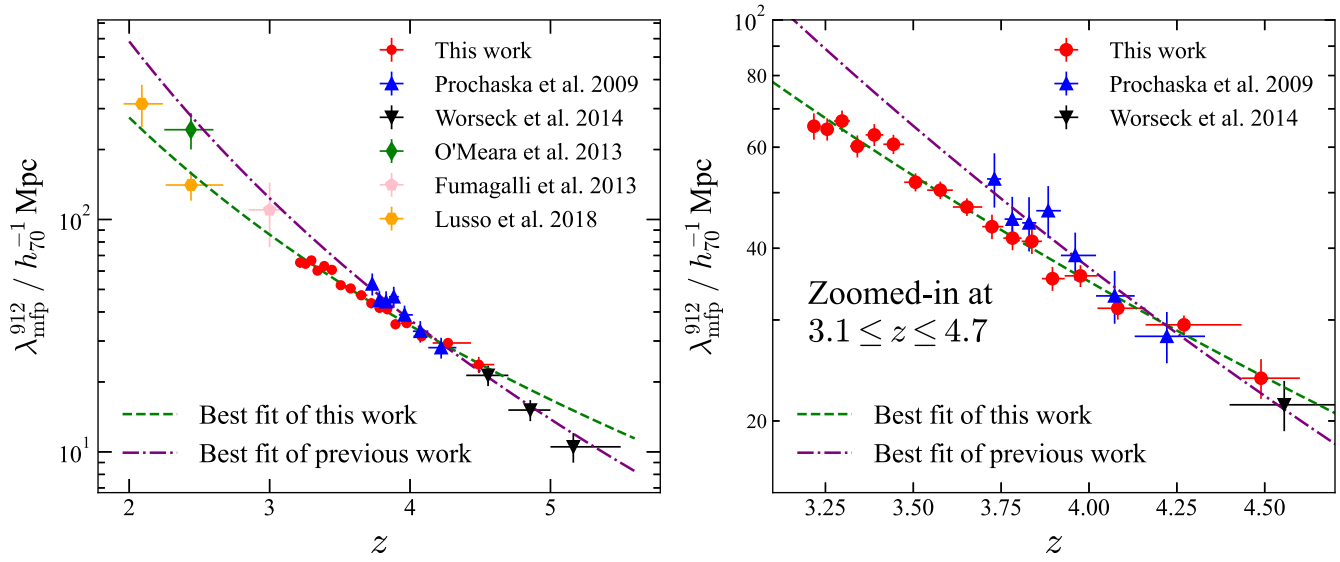

Figure 3. The measured mean free path as a function of redshift, using the T02 SED. Left: the overall mean free path evolution at $2 \lesssim z \lesssim 5$, with data points from P09 (blue upward triangles), M. Fumagalli et al. (2013; pink pengatons), J. M. O'Meara et al. (2013; green diamonds), W14 (black downward triangles), E. Lusso et al. (2018; orange hexagons), and this work (red circles). The violet dashed–dotted line and the green dashed line represent the best power-law fittings in W14 and this work, respectively. Right: the zoom-in plot at $3.1 \leqslant z \leqslant 4.7$, to better display the differences between our work and P09. Our measurements are systematically lower than the interpolation of the W14 power law at $z \lesssim 4$, which is mainly due to the improper handling of the Lyman-series opacity evolution in P09, and our power law is roughly consistent with other previous works.

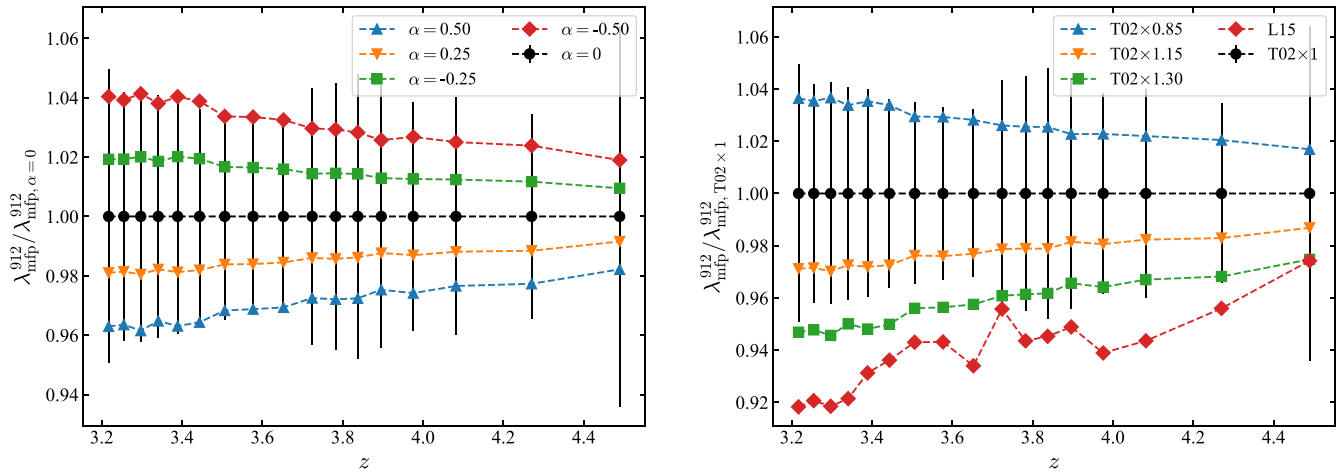

Figure 4. Measurements of different quasar SEDs compared with our default model. Left: measurements when we adjust the tilt index α in Equation (3) to 0.5 (blue upward triangles), 0.25 (orange downward triangles), −0.25 (green squares), and −0.5 (red hexagons), which show that except for an extreme tilt ($|\alpha| \gtrsim 0.5$), our default measurements would not bias more than 5% due to an incorrect spectral index. Right: measurements with different overall normalization. The blue upward triangles, orange downward triangles, and green squares represent the measurements when we shift the T02 SED by 0.85, 1.15, and 1.30. For comparison, we also draw the measurements with L15, represented by the red hexagons. The difference between the L15 and T02 measurements can then be explained for ∼70% by the overall height of the SED, and the remaining ∼30% may come from the shape fluctuations.

4.2. Validations of Systematics

To further investigate the sources of difference in Figure 3, we conduct various validations of our fitting method.

One of the most prominent sources of systematics comes from the choice of quasar SED, which is highly influenced by the sample selection and the method of IGM absorption correction. Parameterizing the SED as $f_\nu \propto \nu^{\alpha_\nu}$, various studies show a similar spectral index α_ν in the Lyman-continuum region. The quasar spectrum composite from T02 with a sample of 184 quasars and a median redshift $z \simeq 1.2$ has a spectral index $\alpha_\nu = -1.76 \pm 0.12$ at wavelength $500 \sim 1200$ Å, and L15 measured a similar result $\alpha_\nu = -1.70 \pm 0.61$ at $z \simeq 2.4$. Other measurements, however, give different indices. M. L. Stevans et al. (2014) exploit the spectra of 159 active galactic nuclei at a median redshift $z \simeq 0.37$ observed with HST/Cosmic Origins Spectrograph and give $\alpha_\nu = -1.41 \pm 0.15$. Z.-Y. Cai & J.-X. Wang (2023) report a more extreme spectral index $\alpha_\nu = -2.4 \pm 0.1$, after correcting the quasar selection bias. Thus, it is necessary to assess the systematic bias induced by the uncertainty of the spectral index. By altering the tilt factor α in Equation (3), we can change this spectral index without changing the overall level of the SED. We show our measurements with different α in the left panel of Figure 4, which indicates that unless the true underlying SED exhibits an extreme spectral index and differs by more than 0.5, our measurements would not be biased by more than 5%, which is of the same scale as the statistical uncertainty, as shown in Figure 4. It is then clear that if we

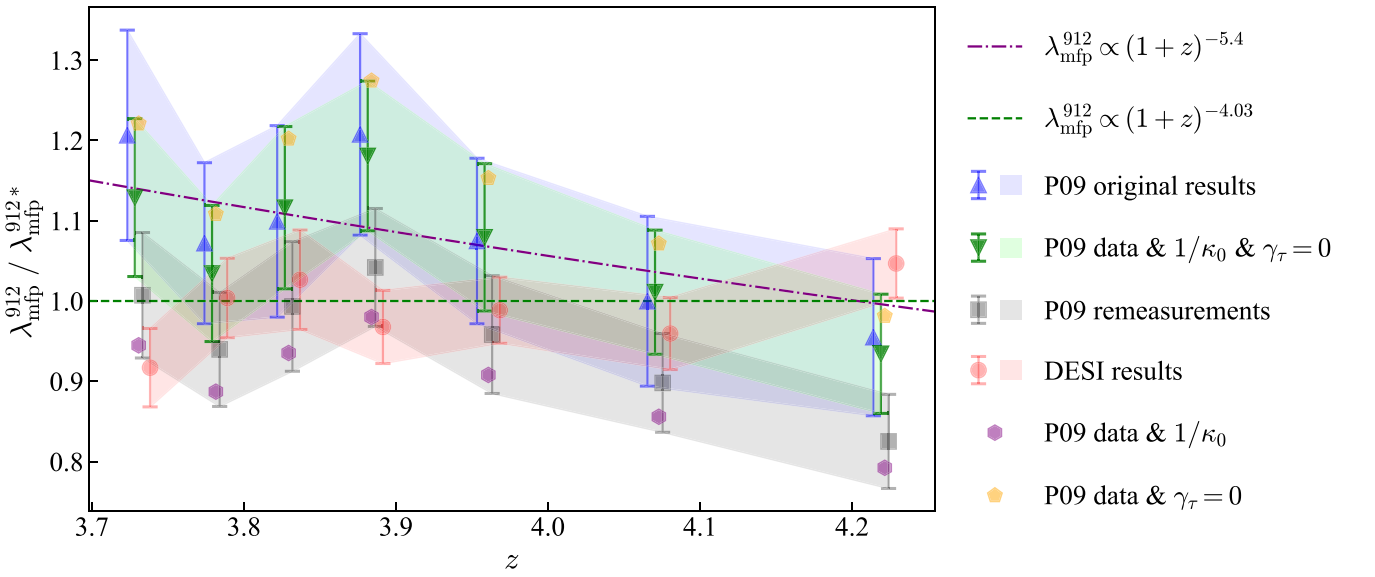

Figure 5. Comparison between different $\lambda_{\rm mfp}^{912}$ measurements. All the points and lines are normalized with our T02 power-law fitting in Table 1 (denoted as $\lambda_{\rm mfp}^{912*}$ on the y-axis label) and are slightly shifted along the x-axis for a better display. The purple dashed–dotted line and green dashed line are the W14 power-law model and our $\lambda_{\rm mfp}^{912*}$ model. The blue upward triangles are the original P09 results. With exactly the same data, we use our method (gray squares), our method with the $\lambda_{\rm mfp}^{912}$ definition as $1/\kappa_0$ (purple pentagons), our method with $\gamma_\tau = 0$ (orange hexagons), and our method with both the $1/\kappa_0$ definition and $\gamma_\tau = 0$ (green downward triangles), respectively, to measure $\lambda_{\rm mfp}^{912}$. Measurements with DESI stacks at the same redshift range are shown with red circles, for comparison. To better illustrate the uncertainty estimates, the blue, green, gray, and red dots are shaded with the same color within the 1σ range, while the purple and orange dots are not. Comparing the blue and green triangles, we believe that our method stays consistent with previous works in estimating both values and uncertainties. Correcting the γ_τ choice makes the P09 measurements consistent with ours (gray squares), while the $z = 4.07$ and $z = 4.22$ results deviate from our $\lambda_{\rm mfp}^{912*}$ model for more than 1σ. The different $\lambda_{\rm mfp}^{912}$ definition would generate $\sim$7% bias, and neglecting γ_τ would bias the result for $\sim$20%.

want to explain the discrepancy with the SED slope, we would have to choose a slope that will contradict most of the previous measurements.

Another source of systematics is the overall level of the SED at the Lyman continuum. Although T02 and L15 have nearly the same spectral index, their overall level differs by $\sim$30% in the Lyα forest when normalized at 1450 Å, as shown in Figure 2. Other SED templates have the same problem, as summarized in Figure 8 of L15 and Figure 3 of Z.-Y. Cai & J.-X. Wang (2023). This problem mainly comes from the IGM absorption correction, which depends highly on the form of the H I absorber distribution function $f(N_{\rm HI}, z)$. L15 choose the J. X. Prochaska et al. (2014) spline model, and T02 choose an empirical broken power law with parameters from various studies (see their Section 2.2). The effect of the SED's overall level is reflected in the estimation of $\tau_0^{\rm LyS}$ in Equation (4), where a higher level will result in a larger $\tau_0^{\rm LyS}$ and therefore a faster Lyman-series opacity evolution. The right panel of Figure 4 shows our measurements with the T02 SED multiplied by different normalization factors. The result is consistent with our thought: a higher SED will prompt a faster declining of the Lyman-series opacity from the rest-frame Lyman limit to shorter wavelengths, requiring the Lyman-limit opacity to be higher, to compensate for the total absorption. The differences between the measurements using T02 and L15 can then be mostly explained by the higher overall level of the L15 SED, and the remaining difference may come from the different SED fluctuations, e.g., the bump at rest frame $\sim$800 Å in the L15 SED shown in Figure 2. Combining the two uncertainties in the quasar SED, we believe that the systematic bias induced by the SED would not exceed $\sim$10%, which means the SED choice cannot entirely explain the $\sim$25% discrepancy with W14.

Neglecting the Lyman-limit opacity evolution when fitting, i.e., enforcing $\gamma_\kappa = 0$ in Equation (9), may also introduce bias to our model. Most of the previous work at similar redshifts did not consider this evolution (P09; M. Fumagalli et al. 2013; W14; E. Lusso et al. 2018). J. M. O'Meara et al. (2013) fitted this parameter and found a mean value $\gamma_\kappa \simeq 0.4$ and a median value $\gamma_\kappa \simeq 0$ at $z \simeq 2$, which means $\gamma_\kappa = 0$ would be a suitable approximation. To better explore the influence of freeing γ_κ on the mean free path measurements, we use the untilted T02 SED to fit our stacked spectra with a $\gamma_\kappa > 0$ uniform prior. These measurements are shown in Table 2, with an example combined MCMC posterior shown in the lower left panel of Figure 10 in Appendix C, where the results are mostly consistent with the results in Table 1, except that the result of the lowest redshift in Table 2 is not physical, which we believe comes from a wavelength range that is too short to constrain γ_κ. Additionally, most γ_κ fittings also deviate from zero, which is not surprising, as the mean free path also evolves quickly at these redshifts. In conclusion, neglecting γ_κ would not bias our measurements, so we continue to keep $\gamma_\kappa = 0$ hereafter.

After the above considerations, we believe that the reason why our measurements are systematically lower than the power law in W14, or in P09, more specifically, is the neglect of the Lyman-series opacity evolution in P09. In other words, P09 simply replace the Lyman-series opacity blueward of 912 Å with $\tau_0^{\rm LyS}$ (Equation (4)), which is estimated at exactly 912 Å. By this means, they overestimated the Lyman-series opacity, leading to an overestimation of the mean free path. To test our idea, we use exactly the same data in P09 and add the $\gamma_\tau = 3$ evolution to remeasure the mean free path, shown in Figure 5 (purple pentagons), together with the original value in P09 (blue upward triangles). Comparing the two sets of data, the neglect of the Lyman-limit opacity evolution could produce

a discrepancy of more than 20%, implying this is a major source of the difference. However, correcting this neglect would overcorrect the mean free path results and make them lower than the $\lambda_{\rm mfp}^{912} \propto (1+z)^{-4.03}$ model (Figure 5, purple pentagons versus green dashed line), which indicates the existence of other bias.

We believe the last source of systematic bias is the definition of the mean free path. Different from us, P09 define $\lambda_{\rm mfp}^{912} = 1/\kappa_0$, where κ_0 is the opacity at the redshift of the emission quasars (Equation (7)). Theoretically, the $1/\kappa_0$ definition estimates the opacity at the light emission source, while the $\tau^{\rm LyC}=1$ definition involves the opacity evolution along the travel of the photons, which would take the evolved lower opacity into consideration and generate a higher mean free path. The results shown in Figure 5 support this claim: measurements with the $1/\kappa_0$ definition are indeed lower by 5%–10% than those with the $\tau^{\rm LyC}=1$ definition (orange hexagons versus green downward triangles and gray squares versus purple pentagons). In A. K. Inoue et al. (2014), the authors also explored the differences between different definitions and came to a similar conclusion. Interestingly, the definition choice in P09 partially offsets the impact of setting $\gamma_\tau = 0$, and together they produce the ∼20% discrepancy in the P09 redshift range. Taking the two factors into consideration, our fitting pipeline reproduces the results in P09 (Figure 5, green downward triangles), which further confirms the validity of our method.

To sum up, we assess several possible sources of systematic bias in the mean free path measurements. The uncertainty of the quasar SED, including its spectral index and the overall level at the Lyman continuum, would bias the mean free path results for ∼10%. Given that the precise quasar SED is still under debate, a less biased SED template is needed for future mean free path measurements. The neglect of γ_κ does not introduce bias and is appropriate for most redshift ranges, but the different treatment of γ_τ is the key factor that causes the discrepancy in Figure 3. Different mean free path definitions would also introduce secondary bias into our model. Note that although we have identified the main sources of discrepancy, Figure 5 still shows a slight discrepancy between the P09 original results and our remeasurements at the low-redshift end. We believe this is from other smaller differences in our fitting method, e.g., the treatment of flux uncertainties or as-yet-unidentified systematic errors.

4.3. Revised Redshift Evolution of the Mean Free Path

Combining the direct measurements from M. Fumagalli et al. (2013), J. M. O'Meara et al. (2013), W14, E. Lusso et al. (2018), G. D. Becker et al. (2021), Y. Zhu et al. (2023), the remeasured P09, and our result using the T02 SED, we suggest a broken-power-law parameterization of the redshift evolution of the mean free path, described by

$$\lambda_{\rm mfp}^{912} = \begin{cases} A\left(\dfrac{1+z}{1+z_0}\right)^{\eta_1}, & \text{when } z \leqslant z_0 \\ A\left(\dfrac{1+z}{1+z_0}\right)^{\eta_2}, & \text{when } z > z_0 \end{cases}, \tag{12}$$

where A, z_0, η_1, η_2 are all free parameters. Note that there has not been a satisfying and theoretically inspired functional form to describe the $\lambda_{\rm mfp}^{912}$ evolution at redshift $z \gtrsim 5$, and our choice here is empirical. Our main purpose is to give a constraint for the transition redshift z_0, instead of giving a precise description of $\lambda_{\rm mfp}^{912}$ evolution at $z \gtrsim 5$.

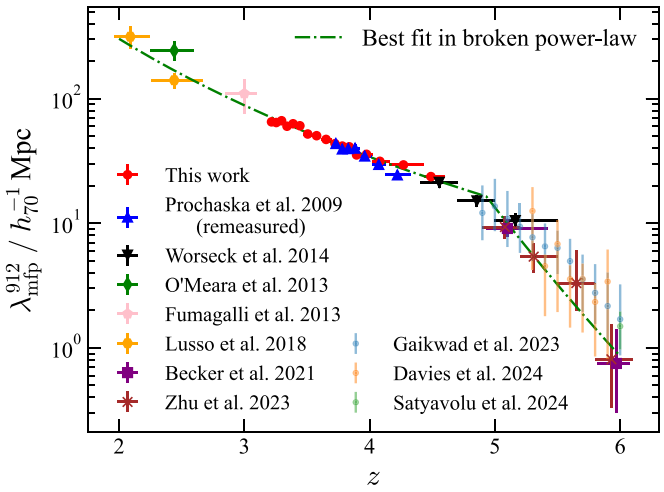

Figure 6. The best-fit broken power law of the current mean free path measurements at $2 \lesssim z \lesssim 6$, using the functional form in Equation (12). The data points in P09 (blue upward triangles) are remeasured using our pipeline, as we do in Figure 5.

With the assumption of Gaussian uncertainty, the best parameter estimates given by the MCMC posterior are $A = 16.51^{+1.85}_{-0.91}\ h_{70}^{-1}$ Mpc, $z_0 = 4.93^{+0.06}_{-0.12}$, $\eta_1 = -4.27^{+0.14}_{-0.12}$, $\eta_2 = -17.73^{+3.13}_{-3.52}$. Figure 6 shows the well-behaved MCMC posterior and the best-fit line that is roughly consistent with all the existing direct measurements of the mean free path. The measurements in P. Gaikwad et al. (2023), F. B. Davies et al. (2024) and S. Satyavolu et al. (2024) in Figure 6 are not included in the fitting, which we will discuss in Appendix E. As the parameter posterior is not Gaussian, we choose the maximum posterior estimates, and the error bars indicate the scaled 1σ range (e.g., if the best estimate corresponds to the 40% quantile, then the lower error bar represents the $(40 \times 16/50)$% quantile and the upper error bar is the $(1\text{–}60 \times 16/50)$% quantile). We stress that we do not correct for the different SEDs of previous works in this fitting: P09, M. Fumagalli et al. (2013), J. M. O'Meara et al. (2013), W14, and our results use the T02 SED, while E. Lusso et al. (2018), G. D. Becker et al. (2021), and Y. Zhu et al. (2023) use the variations of the L15 SED. The fitting would not bias significantly, especially at higher redshift, as we can see that the three independent measurements from W14, G. D. Becker et al. (2021), and Y. Zhu et al. (2023) at $z \simeq 5$ almost coincide with each other. The posterior shows a distinct double-peak feature, but estimates from the two peaks are almost identical and only differ at $z \sim z_0$, so we keep the estimate from the highest peak. We calculate the Bayesian information criterion (BIC) of our broken-power-law model and single-power-law model, defined as

$$\mathrm{BIC} = \chi^2 + p \ln n, \tag{13}$$

where n is the number of data points (37 in this case) and p is the number of parameters (four for a broken power law and two for a single power law). Note that the χ^2 here is computed among the $\lambda_{\rm mfp}^{912}$ measurements and is *not* the one defined in Equation (11). The results show that the broken-power-law model achieves BIC = 51.0, much lower than the single-

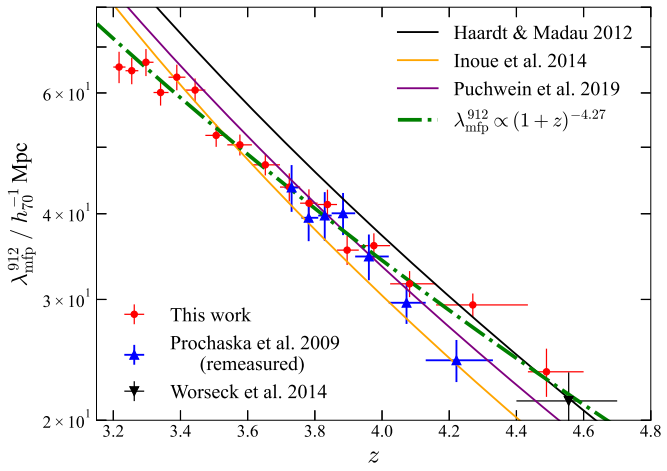

Figure 7. Comparison between our measurements and the previous $f(N_{\rm HI}, z)$ models. The red circles, blue upward triangles and black downward triangles are the observational measurements from our work, the remeasured P09, and W14, respectively. The black, purple, and yellow lines are the mean free path calculations with the Equation (10) definition, using models from F. Haardt & P. Madau (2012), A. K. Inoue et al. (2014), and E. Puchwein et al. (2019), respectively. The green dashed–dotted line represents our best broken-power-law fitting. All three models in the literature overpredict the evolution speed of the mean free path.

power-law model, BIC = 330.7. Our fitting shows that after correcting all the systematics, a slower evolution of the mean free path after $z \simeq 5$ and a break redshift $z_0 = 4.93$ are strongly favored by the existing data.

5. Discussion

5.1. Impact on the Estimation of f(N$_{HI}$, z)

Many empirical estimates of $f(N_{\rm HI}, z)$ have been proposed to study the IGM opacity and provide a theoretical ingredient to calculate the EUVB. We compare the measurements in this work with the most widely used models in the literature—F. Haardt & P. Madau (2012), A. K. Inoue et al. (2014), and E. Puchwein et al. (2019)—in Figure 7, with the z_{912} for calculating $\lambda_{\rm mfp}^{912}$ using Equation (10) defined as

$$\tau^{\rm LyC}(z_{912}, z_{\rm qso}) = \int_0^\infty dN_{\rm HI} \int_{z_{912}}^{z_{\rm qso}} f(N_{\rm HI}, z) \times \{1 - \exp[-N_{\rm HI}\sigma_{\rm ph}(z)]\}\, dz = 1, \quad (14)$$

where $\sigma_{\rm ph}(z)$ is the hydrogen photoionization cross section when the photon reaches redshift z. We do not include the model in C.-A. Faucher-Giguère (2020), as it only differs from E. Puchwein et al. (2019) at low redshift. E. Puchwein et al. (2019; purple line) best match our results among the three models, while F. Haardt & P. Madau (2012) overpredict the mean free path at $z \gtrsim 3.2$. A. K. Inoue et al. (2014) underpredict the mean free path at $z \gtrsim 4$ by ∼15%, with a p-value from an χ^2 goodness-of-fit test of $\sim 1.5 \times 10^{-8}$. Nevertheless, the three models all overpredict the evolution speed implied by our measurements, illustrated with the green dashed–dotted line. However, the functional form in A. Songaila & L. L. Cowie (2010) coincides with our results. All these models are derived from the Lyα absorber statistics, which are easily biased by, e.g., line blending and the clustering of absorption systems (J. X. Prochaska et al. 2010, 2014), while our method does not depend on the specific distribution of Lyα absorbers. Therefore, we encourage a further exploration of systematics and a modification of the form of $f(N_{\rm HI}, z)$ to better match the observations.

5.2. Implications for Reionization

The history of reionization has been studied in a large body of literature with various methods. Measurements of the optical depth of the cosmic microwave background photons set a midpoint for the reionization $z_{\rm re} = 7.82 \pm 0.71$ (Planck Collaboration et al. 2020). Although it was once believed that reionization ends at $z \simeq 6$ (e.g., I. D. McGreer et al. 2015), recent observations of high-redshift quasar spectra provide evidence that reionization may extend significantly below $z \simeq 6$. The long dark gap statistics in Lyα and Lyβ forests strongly rule out a scenario with a homogeneous UV background and a reionization fully completed at $z > 6$ (Y. Zhu et al. 2021, 2022). Measurements of the Lyα effective optical depth and its fluctuations further confirm the judgment and imply an ending that could be as late as $z \simeq 5.3$ (e.g., G. Kulkarni et al. 2019; J. Yang et al. 2020; T. R. Choudhury et al. 2021; S. E. I. Bosman et al. 2022). The methods of dark pixels (e.g., X. Jin et al. 2023) and damping wings (e.g., D. Ďurovčíková et al. 2024; B. Greig et al. 2024; B. Spina et al. 2024; Y. Zhu et al. 2024) are used to constrain the neutral fraction of the IGM at $5 \lesssim z \lesssim 6$ within the Lyα forest, which is a direct probe of the reionization history.

The measurements of the mean free path could also be an independent probe for reionization. The mean free path is first controlled by the typical size of HII bubbles and evolves rapidly at the beginning of reionization. After the overlapping of these bubbles, the mean free path would then be controlled by the optically thick LLS (P. Madau 2017; N. Y. Gnedin & P. Madau 2022). The redshift evolution of the mean free path can therefore be separated into two stages, as indeed shown by our broken-power-law fitting in Equation (12) and reproduced in numerical simulations (e.g., C. Cain et al. 2021; J. S. W. Lewis et al. 2022). However, the transition redshift $z_0 = 4.93$ that is supposed to be the time of overlapping is later than most previous estimates where the neutral fraction of the IGM is constrained to be $\sim 10^{-4}$ at $z \sim 5.5$ (X. Fan et al. 2023). This mild tension may come from an inappropriate choice of our functional form at $z \gtrsim z_0$, but it is difficult for a more precise model to generate a more consistent transition redshift given the lack of mean free path measurements at $z \gtrsim 5$ and the large uncertainty of the existing results. Nevertheless, the measurements of the Lyα effective optical depth $\tau_{\rm eff}$ may provide supplementary support for our claim. The power-law evolution of $\tau_{\rm eff}$ at $2 \lesssim z \lesssim 5$ has an index $\beta \simeq 3$ (e.g., C.-A. Faucher-Giguère et al. 2008b; G. D. Becker et al. 2013; V. Kamble et al. 2020; P. Gaikwad et al. 2021; J. Ding et al. 2024; W. Turner et al. 2024), while at $z \gtrsim 5$, the evolution becomes much faster, with $\beta \simeq 10$ (e.g., J. Yang et al. 2020; S. E. I. Bosman et al. 2022). This roughly coincides with our $\lambda_{\rm mfp}^{912}$ evolution in both the break redshift and the power-law index at either side. In conclusion, the break of the $\lambda_{\rm mfp}^{912}$ evolution at $z = z_0 = 4.93$ implies that reionization may end at this time, but further evidence and interpretation are still needed to better align with other independent measurements.

6. Conclusion

We have presented new measurements of the mean free path of neutral hydrogen ionizing photons at $3.2 \leqslant z \leqslant 4.6$. We construct the largest quasar sample, containing 12,595 quasars from DESI Y1 observations. By fitting the Lyman continuum of the composite quasar spectra at 17 redshift bins, we obtain the most precise measurements to date, summarized in Table 1. Our results are systematically lower at $z \gtrsim 3$ than the previous power-law interpolation in W14 and show a much shallower evolution speed. We investigate a number of possible biases and conclude that the main reason is the neglect of the evolution of the Lyman-series opacity in P09. Combining with all the previous estimates, we believe that the redshift evolution can be best described by a broken power law, with the break redshift $z_0 = 4.93^{+0.06}_{-0.12}$. This evolution is slower than the predictions from most of the current $f(N_{\rm HI}, z)$ models, and although it is later than most other measurements, the power-law break at $z \approx 5$ may be interpreted as the end of HI reionization. As even larger quasar samples from DESI are coming in the next few years, more precise measurements of $\lambda_{\rm mfp}^{912}$, as well as other quantities, such as $\tau_{\rm eff}$, can be conducted in the future, which we believe will provide tighter constraints on the thermal evolution of the IGM in the post-reionization era.

Acknowledgments

We thank Piero Madau and Frederick B. Davies for their constructive advice. We thank Ting-Wen Lan and Vid Irsic for their helpful comments during the DESI internal review. S.Z. acknowledges support from the National Science Foundation of China (no.12303011).

This research is based upon work supported by the U.S. Department of Energy (DOE), Office of Science, Office of High-Energy Physics, under Contract No. DE-AC02-05CH11231, and by the National Energy Research Scientific Computing Center, a DOE Office of Science User Facility under the same contract. Additional support for DESI was provided by the U.S. National Science Foundation (NSF), Division of Astronomical Sciences, under Contract No. AST-0950945 to the NSF's National Optical–Infrared Astronomy Research Laboratory; the Science and Technology Facilities Council of the United Kingdom; the Gordon and Betty Moore Foundation; the Heising–Simons Foundation; the French Alternative Energies and Atomic Energy Commission (CEA); the National Council of Humanities, Science and Technology of Mexico (CONAHCYT); the Ministry of Science, Innovation and Universities of Spain (MICIU/AEI/10.13039/501100011033), and the DESI Member Institutions: https://www.desi.lbl.gov/collaborating-institutions. Any opinions, findings, and conclusions or recommendations expressed in this material are those of the author(s) and do not necessarily reflect the views of the U. S. National Science Foundation, the U. S. Department of Energy, or any of the listed funding agencies.

The authors are honored to be permitted to conduct scientific research on Iolkam Du'ag (Kitt Peak), a mountain with particular significance to the Tohono O'odham Nation.

The data for tables and figures and the code we used are both available in Zenodo: doi:10.5281/zenodo.14167714.

Appendix A
Examples of Spectra

To better illustrate the uncertainty level of our composite spectra, we show examples of the bootstrap spectra in Figure 8. The redshift is chosen to be the same as in Figure 2. We also show the spectra redward of Lyman-α in the right panels of Figure 8, together with SED templates.

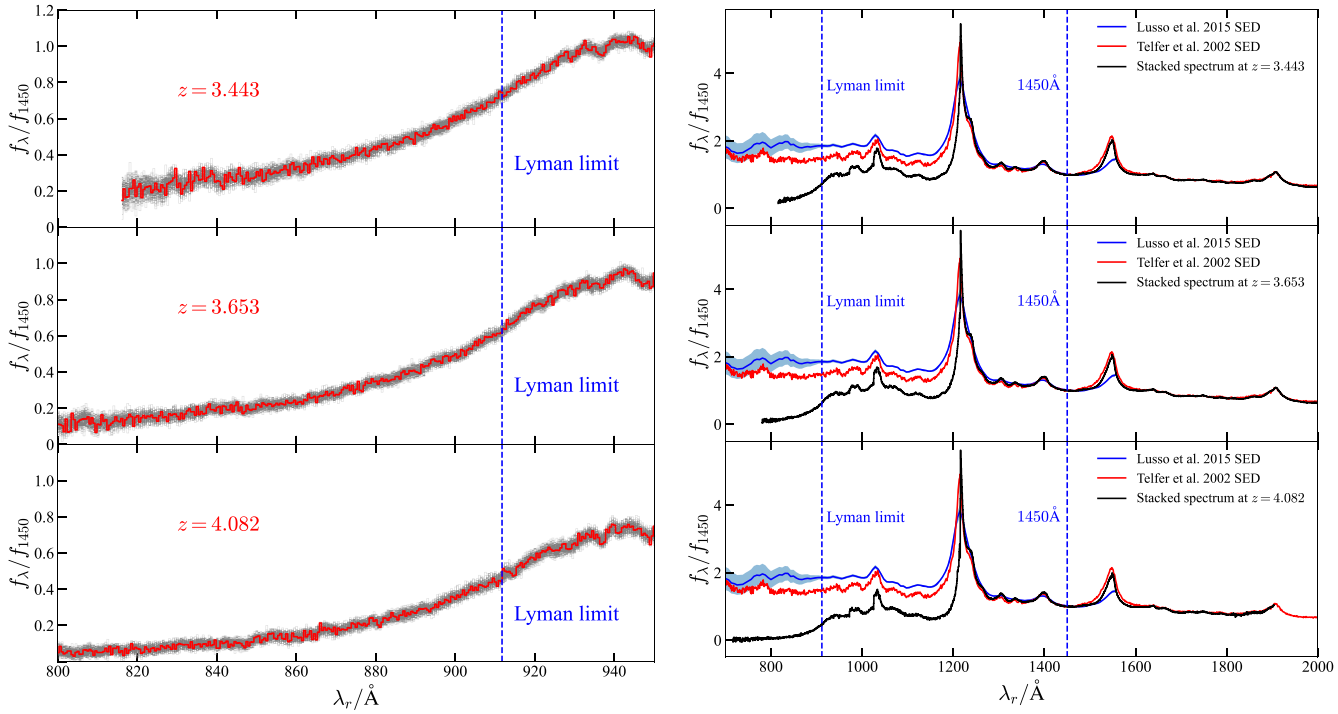

Figure 8. Left: examples of the composite spectra from the bootstrap technique (gray), together with the composite spectra from the normal stacking procedure (red). Right: comparisons between the SED templates and our composite spectra at 700 Å $\leqslant \lambda_r \leqslant$ 2000 Å.

Appendix B
Lyman-series Opacity Evolution

In Equation (4), we approximate the Lyman-series opacity using a power law, and the index γ_τ is chosen to be 3. Figure 9 shows the comparison between our $\gamma_\tau = 3$ approximation and the Lyman-series opacity calculated with the J. X. Prochaska et al. (2014) model, which shows only $\lesssim$1% difference, indicating that $\gamma_\tau = 3$ is a suitable approximation.

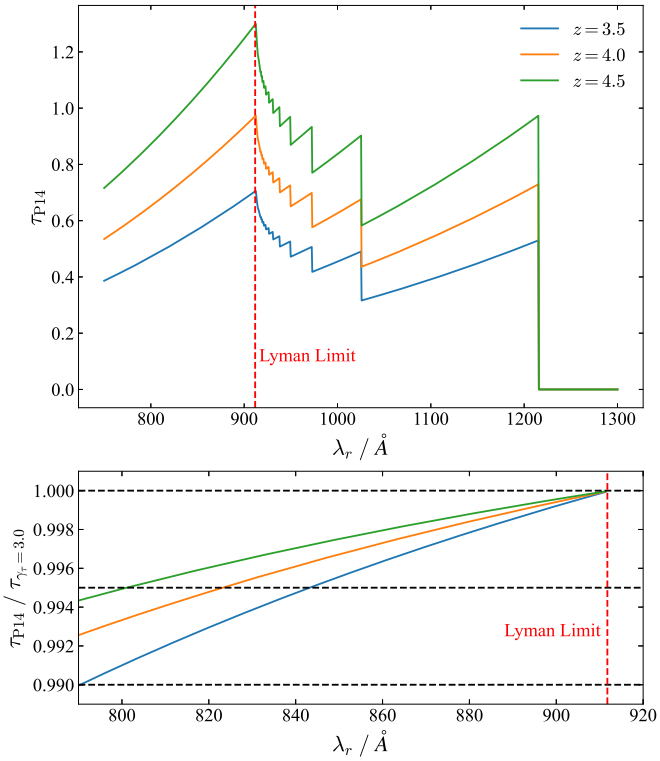

Figure 9. The Lyman-series optical depth calculated using the $f(N_{\rm HI}, z)$ model in J. X. Prochaska et al. (2014; P14), at the rest frame of three z = 3.5 (blue), 4.0 (orange), and 4.5 (green) quasars. The upper panel shows the optical depth accounting for all Lyman-series lines. The lower panel shows the ratio of the optical depth calculated from the P14 model and our Equation (4), with the black horizontal dashed lines representing 1.000, 0.995, and 0.990 and the red vertical dashed line representing the Lyman-limit wavelength (912 Å). The Lyman-series opacity blueward of the Lyman-limit wavelength clearly evolves, and our approximation of the Lyman-series optical depth in Equation (4) is shown to produce only <1% systematic error, and for most cases <0.5%.

Appendix C
Corner Plots of MCMC Posteriors

In this section, we plot the corner plots of all the major MCMC sampling we conducted in Figure 10. The top panels show an example of fitting the composite spectra with our default model. The lower left panel shows an example of fitting with γ_κ in Equation (2) freed. The lower right panel shows the sampling of four parameters in our broken-power-law fitting in Figure 6.

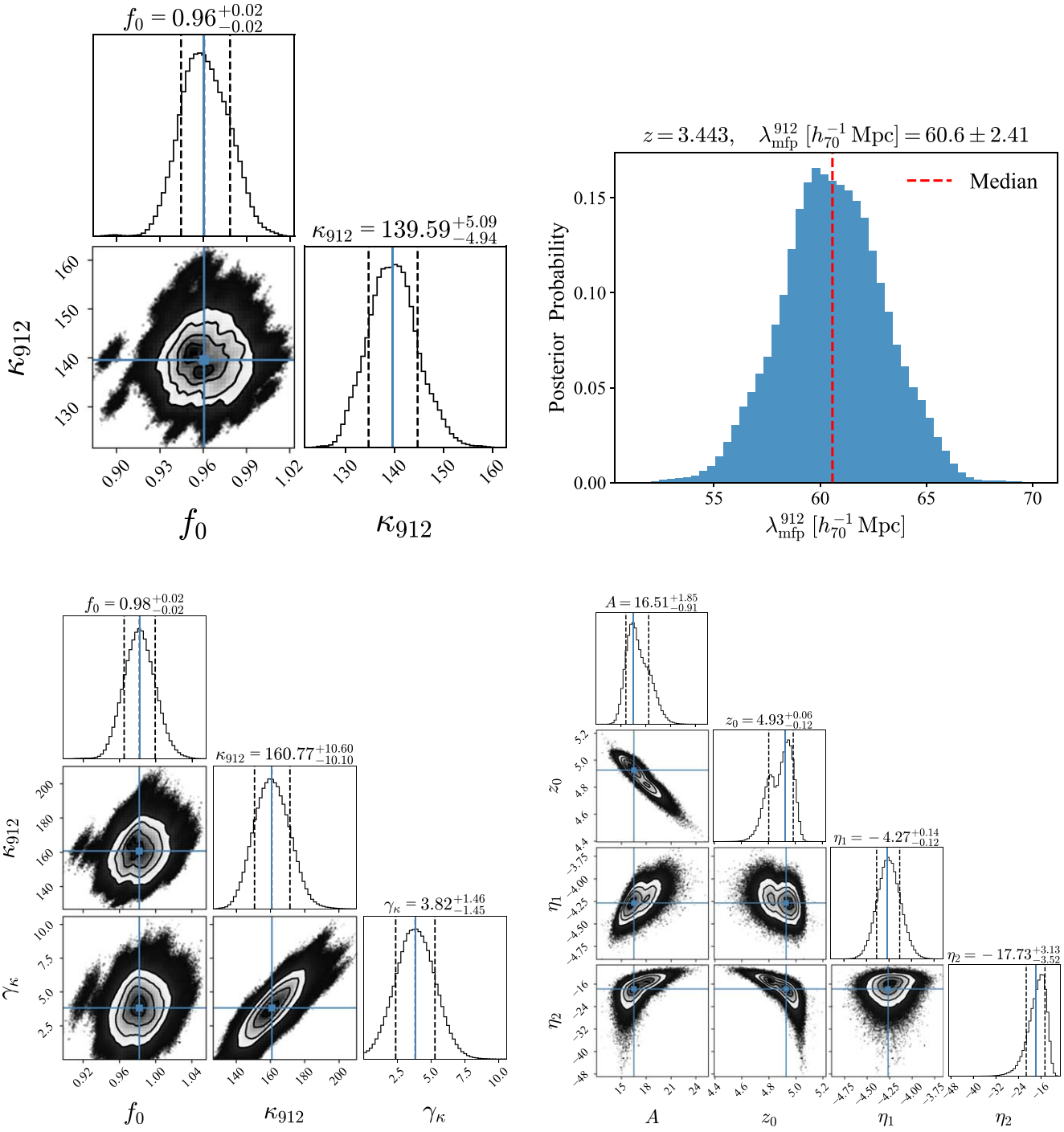

Figure 10. MCMC posteriors. Top left: the combined MCMC sampling of the parameter posterior for the $z_{\rm median} = 3.443$ composite spectrum. The blue lines show the median parameter values in marginal distributions that can be used as appropriate choices for the maximum posterior estimation. The dashed vertical lines denote the 16% and 84% quantiles. Top right: the mean free path distribution calculated from the parameter posterior sample in the top left panel, which is mostly Gaussian-shaped. Lower left: the parameter posterior at $z_{\rm median} = 3.443$ when the parameter γ_κ in Equation (4) is freed. Lower right: the broken-power-law parameter posterior when fitting the data points in Figure 6.

Appendix D
Previous Estimates of $\lambda_{\rm mfp}^{912}$

We compare our results with previous estimates that use a similar method to ours, listed in Table 3. We do not use the results from F. B. Davies et al. (2024), P. Gaikwad et al. (2023), and S. E. I. Bosman (2021), as their methods are significantly different from ours, which may introduce unknown biases. We also do not use other early works that first estimate $f(N_{\rm HI}, z)$ and calculate $\lambda_{\rm mfp}^{912}$ using Equation (14) (e.g., G. C. Rudie et al. 2013), as they suffer from biases, such as line blending and absorber clustering (J. X. Prochaska et al. 2014).

Table 2
γ_κ and $\lambda_{\rm mfp}^{912}$ Measurements when Freeing γ_κ

$z_{\rm median}$	γ_κ	$\lambda_{\rm mfp}^{912}$
3.217	$11.56^{+3.79}_{-3.67}$	439.4 ± 5.88
3.255	0.00 + 0.68	65.4 ± 3.10
3.297	0.00 + 2.28	68.1 ± 3.45
3.341	$3.81^{+1.92}_{-1.77}$	61.0 ± 2.93
3.389	$3.07^{+1.75}_{-1.65}$	63.9 ± 3.01
3.443	$3.82^{+1.46}_{-1.45}$	60.3 ± 2.71
3.506	$2.82^{+1.16}_{-1.23}$	50.9 ± 2.14
3.577	$2.29^{+1.08}_{-1.14}$	49.2 ± 1.91
3.653	$2.93^{+1.11}_{-1.07}$	45.3 ± 1.83
3.724	$3.72^{+1.38}_{-1.45}$	41.2 ± 2.22
3.782	$2.53^{+1.45}_{-1.42}$	39.5 ± 2.17
3.837	$4.02^{+1.30}_{-1.29}$	38.1 ± 2.20
3.896	$2.22^{+1.36}_{-1.29}$	33.9 ± 1.87
3.976	0.00 + 0.99	35.1 ± 1.64
4.082	$1.69^{+1.26}_{-1.12}$	30.5 ± 1.53
4.270	0.00 + 0.50	29.1 ± 1.22
4.489	0.00 + 3.25	22.1 ± 2.06

Note. The unit of $\lambda_{\rm mfp}^{912}$ is h_{70}^{-1} Mpc. Since we applied the $\gamma_\kappa > 0$ prior, the γ_κ estimates with their posterior peaking at $\gamma_\kappa = 0$ are underlined, and their uncertainties are the 50% quantile. Other posteriors peak at nearly 50%, so the upper and lower uncertainties are chosen to be the 84% and 16% quantiles.

Table 3
$\lambda_{\rm mfp}^{912}$ Measurements from Literature

$z_{\rm qso}$	$N_{\rm qso}$	$\lambda_{\rm mfp}^{912}$	$\sigma(\lambda_{\rm mfp}^{912})$	Reference
2.09	48	314.5	64.9	E. Lusso et al. (2018) (Low-z sample)
2.44	46	140.7	20.2	E. Lusso et al. (2018) (High-z sample)
2.44	53	235.8	40.3	J. M. O'Meara et al. (2013)
3.00	61	110.0	34	M. Fumagalli et al. (2013)
3.73	150	52.8	5.7	P09
3.78	150	45	4.2	P09
3.83	150	44.3	4.8	P09
3.88	150	46.5	4.8	P09
3.96	150	38.9	3.7	P09
4.07	150	33	3.5	P09
4.22	150	28.1	2.9	P09
4.56	57	22.2	2.3	W14
4.86	49	15.1	1.8	W14
5.16	39	10.3	1.6	W14
5.08	44	9.33	+2.06/−1.8	Y. Zhu et al. (2023)
5.31	26	5.4	+1.47/−1.40	Y. Zhu et al. (2023)
5.65	9	3.31	+2.74/−1.34	Y. Zhu et al. (2023)
5.93	18	0.81	+0.73/−0.48	Y. Zhu et al. (2023)
5.1	63	9.09	+1.62/−1.28	G. D. Becker et al. (2021)
6.0	13	0.75	+0.65/−0.45	G. D. Becker et al. (2021)

Note. The unit of $\lambda_{\rm mfp}^{912}$ is h_{70}^{-1} Mpc.

Appendix E
Broken-power-law Fitting with More Data

In Section 4.3, we fit the broken-power-law model with the measurements in P09, M. Fumagalli et al. (2013), J. M. O'Meara et al. (2013), W14, E. Lusso et al. (2018), G. D. Becker et al. (2021), Y. Zhu et al. (2023), and our results. In P. Gaikwad et al. (2023), F. B. Davies et al. (2024), and S. Satyavolu et al. (2024), the authors measured the $\lambda_{\rm mfp}^{912}$ at $5 \lesssim z \lesssim 6$ independently, with various cosmological radiative transfer simulations. As their methods are mostly model-dependent and thus different from the direct methods of others, we do not include their results in our fitting in Section 4.3. Here, we present the broken-power-law fitting when incorporating them and show the MCMC parameter posterior in Figure 11 together with the posterior in Section 4.3. The two posteriors are mostly consistent, and the biggest difference would be that the broken redshift is lowered to 4.8. Another interesting thing about the posterior of z_0 is that the implicit second peak at $z_0 \sim 4.8$ in the original posterior is strengthened and becomes the major peak after including more data, implying that the possibility of $z_0 = 4.80$ cannot be simply excluded, and future data are still needed to distinguish the two cases.

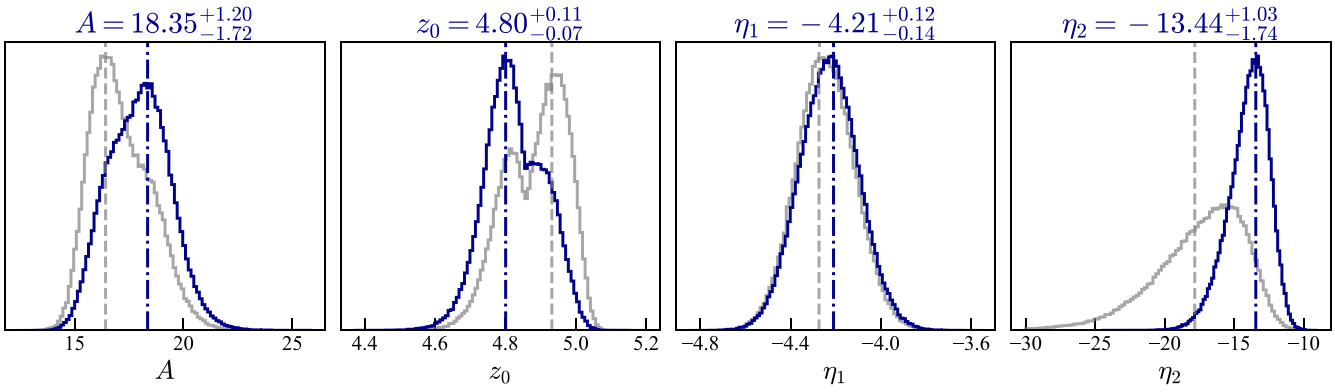

Figure 11. Marginalized parameter posterior of broken-power-law fitting when incorporating data from P. Gaikwad et al. (2023), F. B. Davies et al. (2024), and S. Satyavolu et al. (2024). The blue histograms are the normalized posterior, the blue vertical dashed–dotted lines indicate the maximum posterior estimation, and the blue titles are the parameter estimations, with the uncertainties defined in the way described in Section 4.3. For comparison, we also show the marginalized posterior from Section 4.3 with the gray lines.

ORCID iDs

Anning Gao https://orcid.org/0009-0000-7532-5473
J. Xavier Prochaska https://orcid.org/0000-0002-7738-6875
Zheng Cai https://orcid.org/0000-0001-8467-6478
Siwei Zou https://orcid.org/0000-0002-3983-6484
Cheng Zhao https://orcid.org/0000-0002-1991-7295
Zechang Sun https://orcid.org/0000-0002-8246-7792
S. Ahlen https://orcid.org/0000-0001-6098-7247
D. Bianchi https://orcid.org/0000-0001-9712-0006
D. Brooks https://orcid.org/0000-0002-8458-5047
A. de la Macorra https://orcid.org/0000-0002-1769-1640
Arjun Dey https://orcid.org/0000-0002-4928-4003
P. Doel https://orcid.org/0000-0002-6397-4457
J. E. Forero-Romero https://orcid.org/0000-0002-2890-3725
S. Gontcho A Gontcho https://orcid.org/0000-0003-3142-233X
K. Honscheid https://orcid.org/0000-0002-6550-2023
S. Juneau https://orcid.org/0000-0002-0000-2394
A. Kremin https://orcid.org/0000-0001-6356-7424
P. Martini https://orcid.org/0000-0002-4279-4182
A. Meisner https://orcid.org/0000-0002-1125-7384
R. Miquel https://orcid.org/0000-0002-6610-4836
J. Moustakas https://orcid.org/0000-0002-2733-4559
A. Muñoz-Gutiérrez https://orcid.org/0000-0002-3565-0148
J. A. Newman https://orcid.org/0000-0001-8684-2222
I. Pérez-Ràfols https://orcid.org/0000-0001-6979-0125
E. Sanchez https://orcid.org/0000-0002-9646-8198
D. Sprayberry https://orcid.org/0000-0001-7583-6441
G. Tarlé https://orcid.org/0000-0003-1704-0781
H. Zou https://orcid.org/0000-0002-6684-3997

References

Alexander, D. M., Davis, T. M., Chaussidon, E., et al. 2023, AJ, 165, 124
Anand, A., Guy, J., Bailey, S., et al. 2024, AJ, 168, 124
Becker, G. D., & Bolton, J. S. 2013, MNRAS, 436, 1023
Becker, G. D., D'Aloisio, A., Christenson, H. M., et al. 2021, MNRAS, 508, 1853
Becker, G. D., Hewett, P. C., Worseck, G., & Prochaska, J. X. 2013, MNRAS, 430, 2067
Bolton, J. S., & Haehnelt, M. G. 2007, MNRAS, 382, 325
Bosman, S. E. I. 2021, arXiv:2108.12446
Bosman, S. E. I., Davies, F. B., Becker, G. D., et al. 2022, MNRAS, 514, 55
Busca, N., & Balland, C. 2018, arXiv:1808.09955
Cai, Z.-Y., & Wang, J.-X. 2023, NatAs, 7, 1506
Cain, C., D'Aloisio, A., Gangolli, N., & Becker, G. D. 2021, ApJL, 917, L37
Cardelli, J. A., Clayton, G. C., & Mathis, J. S. 1989, ApJ, 345, 245
Chaussidon, E., Yèche, C., Palanque-Delabrouille, N., et al. 2023, ApJ, 944, 107
Choudhury, T. R., Paranjape, A., & Bosman, S. E. I. 2021, MNRAS, 501, 5782
Cowie, L. L., Barger, A. J., & Trouille, L. 2009, ApJ, 692, 1476
D'Aloisio, A., McQuinn, M., Trac, H., Cain, C., & Mesinger, A. 2020, ApJ, 898, 149
Davé, R., Anglés-Alcázar, D., Narayanan, D., et al. 2019, MNRAS, 486, 2827
Davies, F. B., Bosman, S. E. I., Gaikwad, P., et al. 2024, ApJ, 965, 134
DESI Collaboration, Abareshi, B., Aguilar, J., et al. 2022, AJ, 164, 207
DESI Collaboration, Adame, A. G., Aguilar, J., et al. 2024a, arXiv:2404.03000
DESI Collaboration, Adame, A. G., Aguilar, J., et al. 2024b, AJ, 167, 62
DESI Collaboration, Adame, A. G., Aguilar, J., et al. 2024c, AJ, 168, 58
DESI Collaboration, Aghamousa, A., Aguilar, J., et al. 2016a, arXiv:1611.00036
DESI Collaboration, Aghamousa, A., Aguilar, J., et al. 2016b, arXiv:1611.00037
DESI Collaboration, Adame, A. G., Aguilar, J., et al. 2025a, JCAP, 2025, 124
DESI Collaboration, Adame, A. G., Aguilar, J., et al. 2025b, JCAP, 2025, 021
Dey, A., Schlegel, D. J., Lang, D., et al. 2019, AJ, 157, 168
Ding, J., Madau, P., & Prochaska, J. X. 2024, MNRAS, 532, 2082
Ďurovčíková, D., Eilers, A.-C., Chen, H., et al. 2024, ApJ, 969, 162
Fan, X., Bañados, E., & Simcoe, R. A. 2023, ARA&A, 61, 373
Fan, X., Strauss, M. A., Becker, R. H., et al. 2006, AJ, 132, 117
Faucher-Giguère, C.-A. 2020, MNRAS, 493, 1614
Faucher-Giguère, C.-A., Lidz, A., Hernquist, L., & Zaldarriaga, M. 2008a, ApJ, 688, 85
Faucher-Giguère, C.-A., Lidz, A., Zaldarriaga, M., & Hernquist, L. 2009, ApJ, 703, 1416
Faucher-Giguère, C.-A., Prochaska, J. X., Lidz, A., Hernquist, L., & Zaldarriaga, M. 2008b, ApJ, 681, 831
Filbert, S., Martini, P., Seebaluck, K., et al. 2024, MNRAS, 532, 3669
Fumagalli, M., O'Meara, J. M., Prochaska, J. X., & Worseck, G. 2013, ApJ, 775, 78
Gaikwad, P., Haehnelt, M. G., Davies, F. B., et al. 2023, MNRAS, 525, 4093
Gaikwad, P., Srianand, R., Haehnelt, M. G., & Choudhury, T. R. 2021, MNRAS, 506, 4389
Gnedin, N. Y., & Madau, P. 2022, LRCA, 8, 3
Greig, B., Mesinger, A., Bañados, E., et al. 2024, MNRAS, 530, 3208
Gunn, J. E., & Peterson, B. A. 1965, ApJ, 142, 1633
Guy, J., Bailey, S., Kremin, A., et al. 2023, AJ, 165, 144
Haardt, F., & Madau, P. 1996, ApJ, 461, 20
Haardt, F., & Madau, P. 2012, ApJ, 746, 125
Hall, P. B., Anderson, S. F., Strauss, M. A., et al. 2002, ApJS, 141, 267
Inoue, A. K., Shimizu, I., Iwata, I., & Tanaka, M. 2014, MNRAS, 442, 1805
Jiang, L., Ning, Y., Fan, X., et al. 2022, NatAs, 6, 850
Jin, X., Yang, J., Fan, X., et al. 2023, ApJ, 942, 59
Kamble, V., Dawson, K., du Mas des Bourboux, H., Bautista, J., & Scheinder, D. P. 2020, ApJ, 892, 70
Koposov, S. E., Allende Prieto, C., Cooper, A. P., et al. 2024, MNRAS, 533, 1012
Kulkarni, G., Keating, L. C., Haehnelt, M. G., et al. 2019, MNRAS, 485, L24
Lewis, J. S. W., Ocvirk, P., Sorce, J. G., et al. 2022, MNRAS, 516, 3389
Lusso, E., Fumagalli, M., Rafelski, M., et al. 2018, ApJ, 860, 41
Lusso, E., Worseck, G., Hennawi, J. F., et al. 2015, MNRAS, 449, 4204
Madau, P. 2017, ApJ, 851, 50
Madau, P., & Haardt, F. 2015, ApJL, 813, L8
McGreer, I. D., Mesinger, A., & D'Odorico, V. 2015, MNRAS, 447, 499
Meiksin, A., & Madau, P. 1993, ApJ, 412, 34
O'Meara, J. M., Prochaska, J. X., Worseck, G., Chen, H.-W., & Madau, P. 2013, ApJ, 765, 137
Oppenheimer, B. D., & Davé, R. 2006, MNRAS, 373, 1265
Planck Collaboration, Aghanim, N., Akrami, Y., et al. 2020, A&A, 641, A6
Prochaska, J. X., Madau, P., O'Meara, J. M., & Fumagalli, M. 2014, MNRAS, 438, 476
Prochaska, J. X., O'Meara, J. M., & Worseck, G. 2010, ApJ, 718, 392
Prochaska, J. X., Worseck, G., & O'Meara, J. M. 2009, ApJL, 705, L113
Puchwein, E., Haardt, F., Haehnelt, M. G., & Madau, P. 2019, MNRAS, 485, 47
Rauch, M. 1998, ARA&A, 36, 267
Romano, M., Grazian, A., Giallongo, E., et al. 2019, A&A, 632, A45
Roth, J. T., D'Aloisio, A., Cain, C., et al. 2024, MNRAS, 530, 5209
Rudie, G. C., Steidel, C. C., Shapley, A. E., & Pettini, M. 2013, ApJ, 769, 146
Satyavolu, S., Kulkarni, G., Keating, L. C., & Haehnelt, M. G. 2024, MNRAS, 533, 676
Schaye, J., Crain, R. A., Bower, R. G., et al. 2015, MNRAS, 446, 521
Schlafly, E. F., Kirkby, D., Schlegel, D. J., et al. 2023, AJ, 166, 259
Schlegel, D. J., Finkbeiner, D. P., & Davis, M. 1998, ApJ, 500, 525
Schneider, D. P., Richards, G. T., Hall, P. B., et al. 2010, AJ, 139, 2360
Somerville, R. S., & Davé, R. 2015, ARA&A, 53, 51
Songaila, A., & Cowie, L. L. 2010, ApJ, 721, 1448
Spina, B., Bosman, S. E. I., Davies, F. B., Gaikwad, P., & Zhu, Y. 2024, A&A, 688, L26
Stevans, M. L., Shull, J. M., Danforth, C. W., & Tilton, E. M. 2014, ApJ, 794, 75
Telfer, R. C., Zheng, W., Kriss, G. A., & Davidsen, A. F. 2002, ApJ, 565, 773
Turner, W., Martini, P., GökselKaraçaylı, N., et al. 2024, ApJ, 976, 143
Villasenor, B., Robertson, B., Madau, P., & Schneider, E. 2021, ApJ, 912, 138
Weymann, R. J., Morris, S. L., Foltz, C. B., & Hewett, P. C. 1991, ApJ, 373, 23
Worseck, G., & Prochaska, J. X. 2011, ApJ, 728, 23
Worseck, G., Prochaska, J. X., O'Meara, J. M., et al. 2014, MNRAS, 445, 1745
Yang, J., Wang, F., Fan, X., et al. 2020, ApJ, 904, 26
Zhu, Y., Becker, G. D., Bosman, S. E. I., et al. 2021, ApJ, 923, 223
Zhu, Y., Becker, G. D., Bosman, S. E. I., et al. 2022, ApJ, 932, 76
Zhu, Y., Becker, G. D., Bosman, S. E. I., et al. 2024, MNRAS, 533, L49
Zhu, Y., Becker, G. D., Christenson, H. M., et al. 2023, ApJ, 955, 115